Simulating the impact of extreme sea waves on offshore structures with SPH

R.H.A. IJzermans, A. Thyagarajan, V. Ramohalli Gopala, B.W.H. van Beest, J.M.V.A. Koelman
Shell Technology Centre Bangalore
Bangalore, India
rutger.ijzermans@shell.com

P.K. Pan, K.A. Kochanksi, B.D. Jones, J.R. Williams
Department of Civil & Env Engineering
Massachussetts Institute of Technology
Cambridge, MA, United States of America

***Abstract*— An accurate estimate of forces exerted by extreme sea waves on offshore structures is vital to assess potential risks to structural integrity. The present work describes a methodology to simulate multi-modal and multi-directional sea waves impacting on offshore structures. The waves are generated by moving the side boundaries of the fluid domain according to the sum of random Fourier modes, each with its own direction, amplitude and wave frequency. By carefully selecting the amplitudes and the frequencies, the ensemble of wave modes can be chosen to satisfy a standard sea wave spectrum. We simulate offshore structures as free rigid bodies composed of solid SPH-like particles. Tension-legs are modelled as ideal springs that tether the platform to the sea bed. Elastic collisions between multiple objects are taken into account by an exchange of momentum directed along surface-normal vector of the least convex object at the point of contact. This new collision model does not require any a priori assumption on the shape of the rigid bodies.**

I. INTRODUCTION

Studies of water waves with regular and permanent forms as a fluid dynamical phenomenon have a long history (Stokes, 1847), (Lamb, 1932). The properties of ocean surface waves though, with their random properties and the complex mechanisms of their evolution, are quite different from those of regular water waves. Due to this difference the fundamental studies of ocean surface waves were much delayed. Modern studies of ocean surface waves started in the 1940s with the study by (Sverdrup & Munk, 1947). The most important point of their study was that a sea state can be characterized statistically by a wave spectrum and associated "significant waves", i.e. an average wave height and average wave period.

Extreme waves are defined as waves that have two times higher amplitude than surrounding waves (Liu, Zhang, & Yu, 2011), i.e., much higher than the significant waves in the actual sea state. Reports of extreme waves have circulated for a long time, ever since intercontinental seafaring became common in the 16th Century. For long, the existence of extreme waves was doubted but the existence of extreme waves was unambiguously confirmed on January 1st, 1995, when Statoil's Draupner platform in the Norwegian North Sea recorded an extreme wave of 25.6 m height in an area with significant wave height of approximately 12 metres (Haver, 2004).

A few research groups have performed SPH simulations of extreme wave hitting offshore structures in recent years. For instance, Dominguez [REF] simulated the impact of a solitary wave of elevation on a fixed platform in shallow water, and Rudman & Cleary [REF] modeled the arrival of a single extreme wave on a tension-leg platform. Despite giving an interesting qualitative picture, both studies do not capture some characteristics of real seas, notably the fact that a typical sea state consists of multiple wave modes of different frequencies and different directions.

The present work describes a methodology to simulate multi-modal and multi-directional sea waves impacting on offshore structures. The waves are generated by moving the side boundaries of the fluid domain according to the sum of random Fourier modes, each with its own direction, amplitude and wave frequency. By carefully selecting the amplitudes and the frequencies, the ensemble of wave modes can be chosen to satisfy a standard sea wave spectrum such as the JONSWAP or the Pierson-Moskowitz spectrum [REF].

In order to model the motion of offshore structures correctly, a model for the motion of rigid bodies is required, too. In section II, we will present the rigid-body equations, and we will also discuss a method to take elastic collisions between multiple objects into account. The rigid-body implementation in SPH is validated in a test case presented in section III. Results for the wave elevation in a realistic sea state are presented in section IV. Section V discusses the impact of an extreme wave on offshore structures.

II. PHYSICAL-MATHEMATICAL MODEL

A. *Fluid model in SPH*

We employ a standard implementation of the so-called weakly compressible SPH method (Liu & Liu, 2003). This formulation allows the density of the fluid to vary slightly in the simulation, even if the fluid flow in real-life is virtually incompressible. The pressure is related to the density through an equation-of-state. The numerical speed of sound must be chosen sufficiently large to avoid density fluctuations larger than 1%, but it should be as small as reasonably possible to avoid severe restrictions on the time step.

The local density of each fluid particle is determined using the continuity density formulation (Monaghan, 1994) [REF]. The

equations-of-motion of each fluid particle consist of the standard terms for SPH simulations of fluid (Liu & Liu, 2003) [REF]: a pressure term, a gravity term and artificial viscosity. The equations are numerically stabilized using the standard artificial viscosity formulation (Liu & Liu, 2003) [REF]. In all simulations described in this paper, we have used a value of 0.01 for the dimensionless artificial viscosity parameter α_{AV}.
The force exerted by a boundary particle on a fluid particle is essentially the same as the force between two fluid particles, and consists of the pressure gradient and the viscous force. This is irrespective of whether the boundary particle is a "fixed boundary particle", a "moving boundary particle" or a "floating object particle".
The mass of the boundary particle is chosen in correspondence with the average density of the fluid. The density of the boundary particles is allowed to vary in time. The pressure and density associated with the boundary particle are calculated from the same equations as the fluid particles.

B. Wave generation by moving boundaries

Our goal is to create a sea state that consists of N_{modes} different wave modes with arbitrary wave amplitude, frequency, direction and phase:

$$\zeta(\mathbf{x},t) = \sum_{i=1}^{N_{modes}} A_i \cos\left[\mathbf{k}_i \cdot \mathbf{x} - \omega_i t + \varphi_i\right]. \quad (1)$$

where ζ denotes the free-surface elevation at position $\mathbf{x}$ at time t (here and henceforth, a bold letter denotes a 3D vector). A_i denotes the amplitude of the i-th wave mode, ω_i is the frequency of the i-th wave mode, and φ_i is the phase of the i-th wave mode. $\mathbf{k}_i$ is the dominant wave number of the i-th wave mode. For each mode, the dominant wave number $\mathbf{k}_i$ is related to the wave frequency by the dispersion relation (Lamb, 1932): $\omega_i^2 = g\, k_i \tanh(k_i d)$, where $k_i = |\mathbf{k}_i|$.
The simple summation of wave modes, as described in Equation (1), does not incorporate any effect that one mode may have on the motion of the others. Higher-order methods exist where the mutual interaction is taken into account, within the framework of potential flow theory (Mori & Yasuda, 2002). For the sake of simplicity, we neglect those interactions here. They could be included in a future refinement of the method; there is no conceptual limitation that forces us to look at linear wave interactions here.

The sea state above can be generated by a moving boundary, where each element of the boundary moves according to the following equations-of-motion:

$$\mathbf{u}_{MB} = \sum_{i=1}^{N_{modes}} \frac{A_i \omega_i \mathbf{k}_i}{\chi_i k_i} \cos\left(\mathbf{k}_i \cdot \mathbf{x}_{MB,0} - \omega_i t + \varphi_i\right), \quad \frac{d\mathbf{x}_{MB}}{dt} = \mathbf{u}_{MB} \quad (2)$$

where $\mathbf{x}_{MB,0} = \mathbf{x}_{MB}$ (t = 0). This is a generalization of Havelock's theory to the case of N_{modes} different wave modes, where χ_i denotes the ratio between the wave height far downstream and the stroke of the wavemaker of the i-th wave mode. Havelock (1929) used potential flow theory to derive that χ_i for a single progressive wave is equal to:

$$\chi_{i,\,theory} = \frac{2\left[\cosh(2k_i d) - 1\right]}{\sinh(2k_i d) + 2k_i d}. \quad (3)$$

Ursell (1952) validated Havelock's theory in a lab experiment, and found that the actual wave height is slightly lower than what is predicted by Eq. (3), see Fig. 1. An empirical fit through Ursell's data is:

$$\chi_{i,experiment} \approx 2\tanh\left(\frac{k_i d}{2}\right). \quad (4)$$

This experimental fit is also in agreement with numerical simulations that we performed ourselves in SPH, for exactly the same cases as Ursell. Generally our simulation results are in good agreement with Ursell's measurements. They slightly deviated from Havelock's theory, especially for relatively small wave lengths. Therefore, we decide to employ Eq. (4) in the prescription of moving boundary particles in our SPH simulations of extreme waves.
Havelock's method is expected to work as long as the boundary is far away from the point of interest; Ursell calculated that a horizontal distance equal to 3 times the water depth is sufficient to dissipate any non-linear effects. In the three-dimensional simulations presented in this paper, there is the additional requirement than wave reflections with the boundary must be negligible.

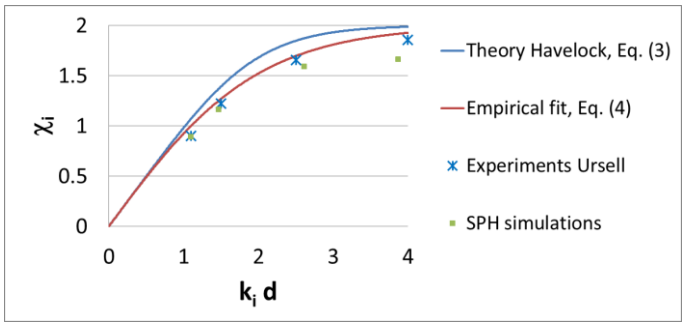

Figure 1. The ratio χ_i between the wave height and the stroke of a wave maker. The blue line denotes Havelock's analytical solution assuming potential flow theory, Eq. (3). The actual experimental data from (Ursell, Dean, & Yu, 1952) are shown as blue stars. Our SPH results for the same cases as Ursell are indicated by green dots. The empirical fit through experimental data from Ursell, given in Eq. (4), is shown in red.

The wave elevation profile given by Eq. (1) only describes a realistic sea state if all the constants are chosen with care. In particular, the following parameters need to be chosen for each wave mode: amplitude A_i, frequency ω_I, wave number vector $\mathbf{k}_i$ (both length and direction), and phase φ_i. A realistic sea state can be modelled by a large number of wave modes, with $N_{modes} > 100$ being common (Liu, Zhang, & Yu, 2011) [REF].
The statistical amplitude distribution is usually described in terms of a wave frequency through a wave spectrum (Faltinsen, 1990). Typical examples are the JONSWAP and the Pierson-Moskowitz spectra. For example, the Pierson-Moskowitz spectrum has the following functional form:

$$S(\omega) = \frac{S_{peak}}{\exp(-5/4)}\left(\frac{\omega_{peak}}{\omega}\right)^5 \exp\left[-\frac{5}{4}\left(\frac{\omega}{\omega_{peak}}\right)^4\right]. \quad (5)$$

where S_{peak} denotes the maximum value of the wave spectrum and ω_{peak} the wave frequency at which the spectrum is maximum. The dimension of the spectrum function $S(\omega)$ is $[m^2 / (rad/s) = m^2 s]$; it thus describes the power spectrum of the free-surface elevation above the nominal water depth. The significant wave height (H_S) is practically equal to four times the square root of the zeroth-order moment of the wave spectrum.

The wave spectrum is a continuous probability density function that can be discretized by assigning one wave mode to one particular frequency (Liu, 2011). The wave frequencies ω_i can for example be chosen on an equidistant grid in the range between ω_{min} and ω_{max}, where ω_{min} and ω_{max} are chosen such that $S(\omega_{min})$ and $S(\omega_{max})$ are virtually zero. The corresponding amplitudes of each wave mode then follow directly from the wave spectrum (Liu, Zhang, & Yu, 2011) [REF]:

$$A_i = \sqrt{S(\omega_i)\Delta\omega_i} = \sqrt{\tfrac{1}{2}S(\omega_i)[\omega_{i+1} - \omega_{i-1}]}, \quad (6)$$

The length of the wave number vector, $\mathbf{k}_i$, is directly related to the wave frequency through the dispersion relation. The directionality of the wave vector $\mathbf{k}_i$ can be obtained by randomly sampling the angle θ_i with respect to the x-axis from a normal distribution with mean θ_0 and variance σ_θ.

In a totally random sea state, the phase is a random number with a uniform distribution between $-\pi$ and π. Occasionally, however, many of the independent wave modes may peak at one point in space at a certain moment in time. This gives rise to an extreme wave, sometimes called a 'rogue wave' or a 'freak wave'.

In a simulation or an experiment, one could in principle wait for the rare event that the most important wave modes focus in the same point. However, this is an inefficient method, as it takes a lot of time, and also the freak wave that occurs does not necessarily occur at a location of interest. An extreme wave event can be generated more efficiently by judiciously choosing the phase of each wave mode (Swan & Latheef, 2013). Thus, we can rewrite Eq. (1) for the elevation profile as:

$$\zeta(\mathbf{x}, t) = \sum_{i=1}^{N_{modes}} A_i \cos[\mathbf{k}_i \cdot (\mathbf{x} - \mathbf{x}_f) - \omega_i (t - t_f) + \tilde{\varphi}_i], \quad (7)$$

where $\tilde{\varphi}_i$ is a modified phase, and $\mathbf{x}_f$ and t_f are the spatial coordinate and the time instant of the extreme wave event, respectively. Note that both $\omega_i t_f$ and $\mathbf{k}_i \cdot \mathbf{x}_f$ only provide a constant phase shift in the cosine.

In order to generate an extreme wave, $\tilde{\varphi}_i$ needs to be chosen within a restricted range close to 0 for sufficiently large portion of wave modes i. In the present study, we choose each $\tilde{\varphi}_i$ as a random number, drawn from a uniform probability distribution between $-\pi/4$ and $\pi/4$. Thus, a high free-surface elevation can be expected at the focus point $\mathbf{x}_f$ at time t_f.

C. Rigid body equations

As a rigid body moves through space, it may translate and rotate. In the mathematical description of rigid body motion, it is convenient to work with two different reference frames: a *world* frame, which remains fixed in time, and an *object* frame which moves and rotates with the object. It is convenient to let the origin of the object frame coincide with the centre-of-mass of the rigid body at all times. Any coordinate in the object frame, $\boldsymbol{\xi}$, can be translated into world frame coordinates $\mathbf{x}$ as follows:

$$\mathbf{x} = \mathbf{r} + [R]\boldsymbol{\xi}. \quad (8)$$

where $\mathbf{r}$ is the position of the centre-of-mass in the world frame, and [R] is the so-called rotation matrix (Meriam & Kraige, 1992). The rotation matrix is composed of the projections of the unit vectors $\mathbf{e}_\xi$, $\mathbf{e}_\eta$, $\mathbf{e}_\zeta$ onto the world coordinate axes x, y and z. Any vector that is defined in the object frame can be expressed as a vector in the world frame by multiplying it with [R].

The displacement $\mathbf{r}$ and the velocity $\mathbf{v}$ of the centre-of-mass of a rigid body are given by:

$$\frac{d\mathbf{r}}{dt} = \mathbf{v}, \qquad \frac{d\mathbf{v}}{dt} = m^{-1}\mathbf{F}. \quad (9)$$

where $\mathbf{F}$ represents the total external force on the rigid body. In our simulations, the force $\mathbf{F} = \mathbf{F}_f + \mathbf{F}_g + \mathbf{F}_t$ where $\mathbf{F}_f$ denotes the force from the fluid on the object, $\mathbf{F}_g$ is the gravitational force, and (in the case of a tension-leg platform) $\mathbf{F}_t$ is an additional spring force from each tension leg.

In the object frame, the angular momentum vector $\mathbf{M}$ of a rigid body is equal to the vector-multiplication of the moment-of-inertia tensor [I] and the angular velocity $\boldsymbol{\omega}$: $\mathbf{M} = [I]\boldsymbol{\omega}$, where both [I] and $\boldsymbol{\omega}$ are defined in the object frame. In the world frame, however, the angular momentum vector $\mathbf{L}$ is the multiplication of [R] and $\mathbf{M}$:

$$\mathbf{L} = [R]\mathbf{M} = [R][I]\boldsymbol{\omega}. \quad (10)$$

For rotating rigid bodies, [I] is constant in time, but [R] is not. The change of angular momentum in the world frame in time is equal to the external torque $\mathbf{T}$ applied. The external torque $\mathbf{T}$ can either be come from the fluid or (in the case of a tension-leg platform) from the additional spring force from each tension leg. The time change of the angular momentum can be derived from Eq. (10) as:

$$\frac{d}{dt}\mathbf{L} = \mathbf{T} = [R][\Omega][I]\boldsymbol{\omega} + [R][I]\frac{d\boldsymbol{\omega}}{dt}, \quad (11)$$

where we have used that the evolution of the rotation matrix [R] in the course of time is (Bourg & Bywalec,2013):

$$\frac{d}{dt}[R] = [R][\Omega] = [R]\begin{bmatrix} 0 & -\omega_\zeta & \omega_\eta \\ \omega_\zeta & 0 & -\omega_\xi \\ -\omega_\eta & \omega_\xi & 0 \end{bmatrix}, \quad (12)$$

Rewriting Eq. (11) gives an expression for the angular acceleration $d\boldsymbol{\omega}/dt$:

$$\frac{d\boldsymbol{\omega}}{dt} = [I]^{-1}[R]^{-1}\left(\mathbf{T} - [R][\Omega][I]\boldsymbol{\omega}\right). \quad (13)$$

For an accurate solution, the variables **r**, **v**, **ω** and [R] need to be solved simultaneously in the course of time, since their evolution equations are coupled. In addition, the force and torque on the object, **F** and **T**, need to be evaluated at each instant of time.

In our implementation, rigid bodies are composed of SPH particles, too. The force from the fluid on the floating rigid body is calculated from Newton's Third Law ("Action = – Reaction"): it is exactly opposite to the force exerted by the boundary particles in the floating object on the fluid. The torque on the rigid body is calculated from the sum of the individual particle-particle interactions as well.

The calculation routine for the velocity of the center-of-mass of the floating rigid body is on a simple first-order Euler discretization of the acceleration:

$$\mathbf{v}^{n+1} = \mathbf{v}^n + m^{-1}\mathbf{F}\left(t^n\right)\Delta t^n. \quad (14)$$

with **F** evaluated based on the particle positions at the previous time step. Note that the time step Δt may be variable. The displacement is calculated from a trapezium rule, and is second-order accurate:

$$\mathbf{r}^{n+1} = \mathbf{r}^n + \tfrac{1}{2}\left(\mathbf{v}^{n+1} + \mathbf{v}^n\right)\Delta t^n. \quad (15)$$

Also the angular velocity in the object frame is calculated using an explicit Euler scheme:

$$\boldsymbol{\omega}^{n+1} = \boldsymbol{\omega}^n + \Delta t^n\left\{[I]^{-1}[R]^{-1}\left(\mathbf{T} - [R][\Omega][I]\boldsymbol{\omega}\right)\right\}^n, \quad (16)$$

where the variables on the right-hand-side, [R], **T**, [Ω] and **ω**, are all taken from the previous time step, n. The evolution equation of the rotation matrix is determined after the calculation of the angular velocity, with the time-step averaged value of $\boldsymbol{\omega}^{n,av} = (\boldsymbol{\omega}^{n+1} + \boldsymbol{\omega}^n)/2$:

$$[R]^{n^*} = [R]^n + \Delta t^n [R]^n [\Omega]^{n,av}, \quad (17)$$

where n* is a fictitious future time step; $[R]^{n^*}$ is an estimate of the rotation matrix at the new time step. In a second step, the matrix $[R]^{n^*}$ is subject to Gram-Schmidt orthonormalization, with $[R]^{n+1}$ as output. This procedure ensures that $[R]^{n+1}$ is a pure rotation matrix, i.e. it does not cause any translation of the vector it is multiplied with.

Finally, the position of each particle "j" inside the rigid body is specified by:

$$\mathbf{x}_j^{n+1} = [R]^{n+1}\boldsymbol{\xi}_{j,CoM} + \mathbf{r}^{n+1}, \quad (18)$$

and its velocity by:

$$\mathbf{v}_j^{n+1} = \mathbf{v}^{n+1} + [R]^{n+1}\left(\boldsymbol{\omega}^{n+1} \times \boldsymbol{\xi}_{j,CoM}\right), \quad (19)$$

where $\boldsymbol{\xi}_{j,CoM}$ denotes the separation vector, in the object frame, between the particle "j" and the object's centre-of-mass.

D. Collision model

When two solid rigid bodies (labelled '1' and '2') come in contact with each other, they will collide. In this section, we present the equations that describe an elastic collision between two rigid bodies. The collision model is based on the conservation of linear momentum, angular momentum and energy, following the approach described by (Hakenberg, 2008). The point of collision, in world coordinates, is denoted by $\mathbf{r}_c$. The collision detection algorithm is incorporated in the nearest-neighbor search algorithm which is also used to detect particle pairs in the SPH simulation.

During the collision, a force applies for a short period of time that pushes the objects away from each other. Without making any a priori assumption on its magnitude or direction, we denote this force by $\mathbf{F}_{coll}$. Typically, near-elastic collisions take place over a short period of time compared to the time scales of interest of a problem. The total exchange of forces during this short interval can be captured by the collision impulse, $\mathbf{I}_{coll}$, which is equal to:

$$\mathbf{I}_{coll} = \int_{t^-}^{t^+} \mathbf{F}_{coll} dt \cdot \quad (20)$$

Here t^- denotes a time just before the collision and t^+ the time just after the collision. Without loss of generality, we may introduce λ as the collision impulse magnitude and **n** as a unit vector indicating the direction along which the forces are exchanged: $\mathbf{I}_{coll} = \lambda\,\mathbf{n}$.

Integration in time (between t^- and t^+) of the momentum equation of each object gives an expression for the velocity of each object before the collision, $\mathbf{v}_i$, and after the collision, $\mathbf{v}'_i$:

$$\mathbf{v}'_1 = \mathbf{v}_1 - \frac{\lambda}{m_1}\mathbf{n}; \qquad \mathbf{v}'_2 = \mathbf{v}_2 + \frac{\lambda}{m_2}\mathbf{n}. \quad (21)$$

Similarly, integration in time of the angular momentum equation of each object gives an expression for the angular velocity of object i after the collision, $\boldsymbol{\omega}'_i$, in terms of the angular velocity before the collision, $\boldsymbol{\omega}_i$:

$$\boldsymbol{\omega}'_1 = \boldsymbol{\omega}_1 - \lambda\mathbf{q}_1; \qquad \boldsymbol{\omega}'_2 = \boldsymbol{\omega}_2 + \lambda\mathbf{q}_2 \quad (22)$$

where we have introduced the shorthand:

$$\mathbf{q}_i \equiv [I_i]^{-1}[R_i]^{-1}\left(\mathbf{r}_c - \mathbf{r}_i\right) \times \mathbf{n}. \quad (23)$$

If we assume the collision to be perfectly elastic, the value of λ can be directly derived from the conservation of energy. The total energy in the system is composed of kinetic energy and rotational energy of the two objects, and energy conservation gives a second-order polynomial in λ, which has two solutions. One solution is λ = 0, i.e. 'no collision'; the other solution is the one that is relevant for an elastic collision:

$$\lambda = 2\frac{\mathbf{v}_1 \cdot \mathbf{n} - \mathbf{v}_2 \cdot \mathbf{n} + \mathbf{q}_1^T[I_1]\boldsymbol{\omega}_1 - \mathbf{q}_2^T[I_2]\boldsymbol{\omega}_2}{m_1^{-1} + m_2^{-1} + \mathbf{q}_1^T[I_1]\mathbf{q}_1 + \mathbf{q}_2^T[I_2]\mathbf{q}_2}. \quad (24)$$

This expression is exact for any elastic collision, regardless of the precise geometry of the objects, or the magnitude or direction of the collision force $\mathbf{F}_{coll}$.
The only remaining free parameter is the unit vector **n**. It denotes the direction in which the momentum is exchanged between two colliding objects. In a typical collision between two arbitrarily shaped objects, one object will have a wedged shape at $\mathbf{r}_c$ whereas the other object will have a flat surface at $\mathbf{r}_c$. In the present study, we choose **n** as the surface-normal vector of the 'flattest surface'. Thus, all the momentum between the two objects is exchanged in the direction of **n**. The surface-normal vectors at the point of collision are calculated from the positions of nearby particles in the rigid bodies; the 'flattest surface' belongs to the object with the highest number of particles near $\mathbf{r}_c$.

III. VALIDATION FOR RIGID BODY MOTION

We validate our implementation of the rigid body equations against an experiment by Kraskowski (2010), who used it for the validation of a self-developed volume-of-fluid method. Kraskowski's experiment is interesting in that it involves a full three-dimensional rotation of the rigid body.

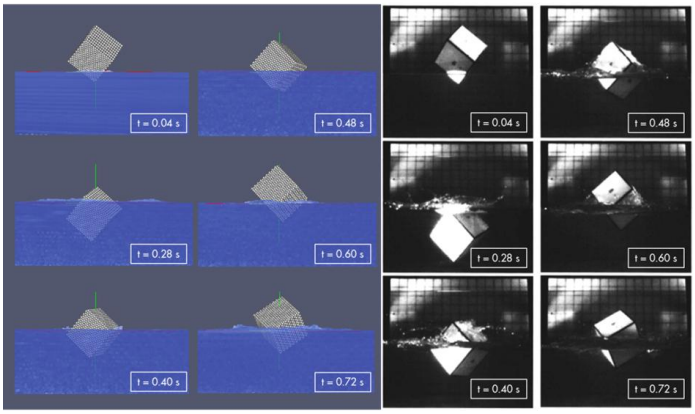

Figure 2. Snapshot of the floating object at six instants of time. Left: SPH simulation. Right: Experiment by Kraskowski. The time is measured after the impact of the floating object on the water surface. The fluid is coloured by velocity magnitude (dark red = 1 m/s, dark blue = 0 m/s).

The experimental setup is as follows. A 150 mm wide cube is freely hanging on a wire above a basin of water, with the lowest corner 5 cm above the water level. The water basin is 1.3 m long, 1.0 m wide and 0.25 m deep. The experiment is carried out in a lab at room temperature. The object is not made of a uniform material, but it has a geometrically eccentric centre-of-mass, 7 mm towards the top face. Further details on the object can be found in Kraskowski (2010).

At the start of the experiment, the wire is cut and the object is allowed to fall into the basin. Due to the eccentricity of the centre-of-mass, the object starts to roll in the water. A high-speed camera is used to register the motion and the orientation of the object at many instants of time.

We simulated Kraskowski's experiment with SPH, with particle size equal to 10 mm. Such a resolution is similar to one used by Ulrich (2013) who considered the same case.

Snapshots from our SPH simulation are shown in Figure 2, where they are compared with pictures from experiment reported by Kraskowski (2010). Our simulation appears to be in very good agreement with the experiment, for what the position and orientation of the object are concerned.

IV. SIMULATION OF EXTREME WAVE

Now we simulate an extreme wave with SPH. The underlying sea state consists of 100 modes of different frequency and direction. First, in section IV, we will analyse the sea state itself; our objective is to accurately reproduce the New Year Wave event. Then, in section V, we will simulate the impact of an extreme wave on a tension-leg platform surrounded by two ships.

A. *Geometry and setup*

The fluid basin is 50 m deep and stretches over a longitudinal distance of 800 m, with a transverse width of 150 m. The beach, which is intended to prevent reflection of waves, starts at 600 m from the left wall of the domain and has an angle of 14° with the horizontal. In the transverse direction, the fluid is contained by solid side walls. The numerical speed of sound in the fluid is chosen as 300 m/s, and the particle size in the simulations presented in this section is 2.25 m.

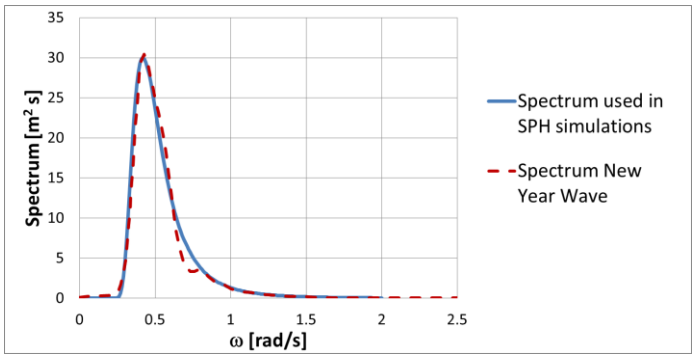

Figure 3. Wave spectrum for New Year Wave (Liu, 2010), and the model wave spectrum used in our SPH simulations.

Waves are generated through the displacement of a part of the vertical side walls by a prescribed motion, in order to generate an extreme wave at x_f = 390 m after t_f = 60 s. The "moving boundary" particles that are displaced with a prescribed motion are plotted as dark grey dots in the 'top view' snapshot of Figure 6. In principle, each of these particles should follow the equation of motion for moving boundary particles, Equation (2), in order to generate the free-surface elevation profile in Equation (1). However, one adjustment needs to be made: if the boundary particles were freely allowed to follow Equation (2), holes would appear in the side wall between the fixed and the moving boundary particles, leading to a leaking of fluid. This is obviously an undesired effect. In order to maintain a continuous boundary without gaps, a transition zone is identified (see Figure 4) where a spatial smoothing is applied. The spatial smoothing factor is of the following form:

$$f_x = \tfrac{1}{2}\left\{1+\tanh\left[7.6\left(\frac{x_{limit}-x}{L_x}-\frac{1}{2}\right)\right]\right\}. \qquad (24)$$

where x_{limit} = 390 m here, and L_x is a smoothing length that we choose equal to 100 m in our simulations.
Similarly, it is not possible in SPH to start moving the boundaries vigorously at time t = 0 s. The reason is that the particles first need to 'settle'; an initial disruption may cause numerical instabilities. Therefore we apply smoothing in time:

$$f_t = \tfrac{1}{2}\left\{1+\tanh\left[7.6\left(\frac{t}{t^*}-\frac{1}{2}\right)\right]\right\}. \qquad (24)$$

where t* is some smoothing time scale. In the present simulations we choose t* equal to 30 s.

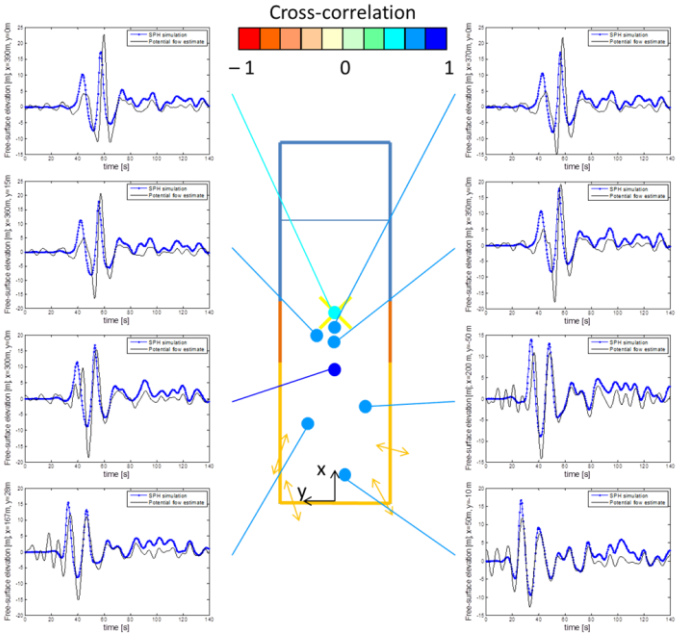

Figure 4. Free-surface profiles from SPH simulation of an extreme wave event. A schematic top view of the domain is drawn in the middle: yellow lines denote side walls composed of "moving boundary" particles, blue lines indicate fixed side walls, and brown lines are the transition region given by Eq. (25). The focal point of the extreme wave is depicted by the yellow cross. A comparison is made with the potential flow estimate from Equation (7), at eight different positions in the domain. The dots and the connecting lines are coloured by the cross-correlation of the SPH simulation data and the potential flow estimate in the interval 60 s < time < 140 s.

Equation (2) for the velocity of any "moving boundary" particle "j" now becomes:

$$\mathbf{u}_{j,MB} = f_x f_t \sum_{i=1}^{N_{modes}} \frac{A_i \omega_i \mathbf{k}_i}{\chi_i k_i} \cos\left[\mathbf{k}_i \cdot \left(\mathbf{x}_{j,MB,0} - \mathbf{x}_f\right) - \omega_i (t - t_f) + \tilde{\varphi}_i\right]. \qquad (24)$$

For each wave mode "i", the amplitude A_i, the wave number $\mathbf{k}_i$, the frequency ω_i, the phase $\tilde{\varphi}_i$ and the direction θ_i can be chosen based on any target wave spectrum, as we described in section II. Here, we use a Pierson-Moskowitz spectrum (Stewart, 2005)) with a maximum peak intensity of 30 m^2 s, at the peak frequency of 0.42 rad/s. This corresponds to the spectrum measured at the Draupner platform during the extreme wave event (Liu, Zhang, & Yu, 2011) [REF], see Figure 3. The spectrum is modelled by 100 independent modes, which are subject to some degree of randomness: the direction of each wave mode is taken from a Gaussian distribution with variance of 15 degrees and the phase of each wave mode is randomly picked from a uniform distribution between – π/4 and π/4. The wave modes combine to form an extreme wave at a given focus point and focus time.

B. Simulation of extreme wave

The result for the free-surface elevation from the SPH simulation is shown in Figure 4, for eight different measurement points in the domain. The results are compared with the expected elevation from potential flow theory for the same case (Equation (7)), with identical data for the amplitudes, phases and wave numbers of each wave mode. The data points are colored by the cross-correlation (Pearson, 1895) [REF] between the SPH simulation result and the potential flow estimate.
In all measurement locations shown in Figure 4, the wave peaks occur at approximately the same time, and the wave heights are generally in reasonable agreement. The cross-correlations between the SPH simulation and the potential flow solution are generally above 70%.
The lowest cross-correlation of 45% occurs at (x, y) = (390 m, 0 m); the main reason is that the height of the extreme wave simulated by SPH is somewhat lower than what is predicted by potential flow theory (18 m vs. 23 m). The difference can be attributed to some excessive numerical diffusion in the SPH simulation on the one hand, and to the limited applicability of linear potential flow theory to describe high waves and breaking waves on the other hand.
Nevertheless, the results demonstrate that it is possible to model an extreme wave in an SPH simulation, more or less at the designated 'focus point' and 'focus time'. In fact, the highest peak in the water elevation in the SPH simulations occurs at x = 350 m at t = 55 seconds, which is not very different from the intended focus point and time ($\mathbf{x}_f$, t_f) = (x = 390 m, y = 0 m; t = 60 s). The peak wave arrives at $\mathbf{x}_f$ a few seconds earlier than t_f because large waves travel faster than small waves. This effect, which is related to the non-linearity of surface waves (Stokes, 1847), is not taken into account in the first-order potential flow theory, but it is implicitly taken into account in the SPH simulation.
The wave height measured at $\mathbf{x}$ = $\mathbf{x}_f$ is shown in Figure 5; the time axis is shifted, so that the peak of the extreme wave occurs at t – t_{peak} = 0 s. There is good agreement with the measured extreme wave, of which the elevation data were given in (Liu, Zhang, & Yu, 2011).

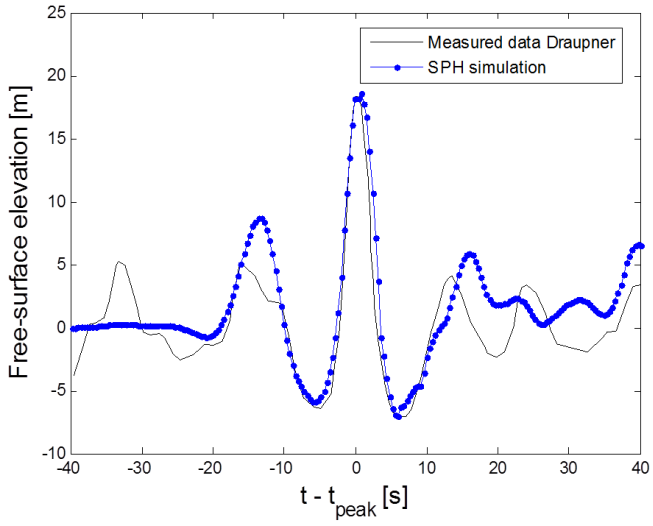

Figure 5. SPH prediction for the wave profile, as measured at the location where the front of the platform is located initially. The target elevation, from Draupner's 'New Year Wave' data, is shown as well.

No particular tuning parameters were used to obtain this result. Apart from the wave spectrum that was taken equal to the measured Draupner spectrum, the only input parameters to the flow model were:

- The number of wave modes: here we took it as 100, to cover the whole range of wave frequencies.
- The phases of wave modes: chosen randomly between $-\pi/4$ and $+\pi/4$, to focus the wave modes in order to generate the extreme wave.
- The standard deviation of the directionality, σ_θ: chosen as 15 degrees, which is a reasonable value for a typical sea state (Ewans & Jonathan, 2008) [REF].

The position and time of focusing is specified through the choice of the phases of the individual wave components. Nothing particular was specified to model what happens before or after the extreme wave. Therefore, the SPH simulation result in Figure 5 is not necessarily in agreement with the measured data a long time before or after the peak event. Nevertheless, the general statistics are reproduced well, especially the troughs before and after the extreme wave.

According to (Liu, Zhang, & Yu, 2011) [REF], any extreme wave can be characterised by four dimensionless parameters:

- The height of the extreme wave (peak + trough) compared to the significant wave height, $\alpha = H_{EW} / H_s$.
- The height of the extreme wave compared to the previous wave peak, $\beta_1 = H_{EW} / H_{EW-1}$.
- The height of the extreme wave compared to the next wave peak, $\beta_1 = H_{EW} / H_{EW+1}$.
- The height of the extreme wave compared to its amplitude above the nominal sea level, $\mu = H_{EW} / \eta_{EW+1}$.

According to the measurement data, these parameters are for the New Year Wave: $\alpha = 2.15$, $\beta_1 = 2.25$, $\beta_2 = 2.5$ and $\mu = 0.72$ (Liu, Zhang, & Yu, 2011). Our SPH simulation predicts the following values: $\alpha = 2.08$ (–3%), $\beta_1 = 2.78$ (+24%), $\beta_2 = 2.12$ (–15%) and $\mu = 0.72$ (+0%). Thus, there seems to be good agreement for these parameters that characterize an extreme wave.

V. EXTREME WAVE ON OFFSHORE STRUCTURES

As a proof-of-concept, we will show a real-life application of the new collision model. We will study the effect of an extreme sea wave hitting a tension-leg platform surrounded by two ships. The method to generate the extreme wave is identical to what was presented in section 4. The front of the platform is initially located at the focusing point of the extreme wave.

A. *Geometry description*

Three rigid bodies are present in the simulation:

- A tension-leg platform ('Object 1').
- One ship with the bow in the direction of the extreme wave ('Object 2').
- One ship with the bow in the direction of the extreme wave ('Object 3').

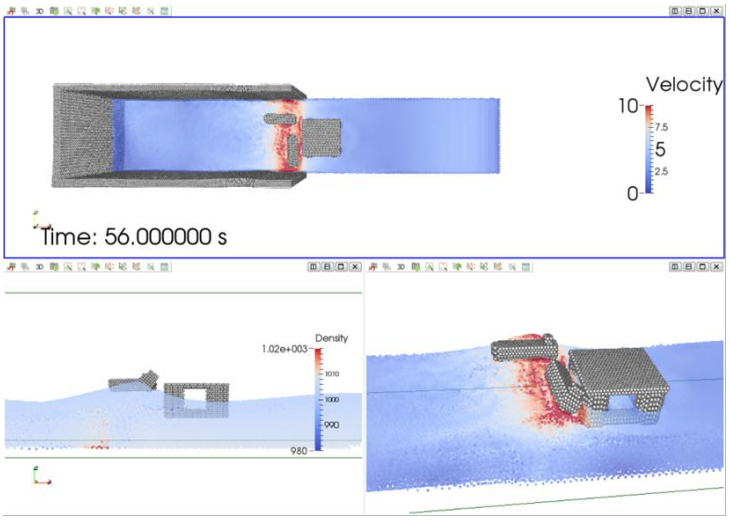

Figure 6. Snapshots of SPH simulation of an extreme wave hitting a tension-leg platform surrounded by two ships. The "moving boundary" particles are shown in grey in the top view. The other, fixed, boundary particles in the side walls are not shown here, to allow a clear view on the offshore structures. Top and bottom right: fluid particles are coloured by velocity magnitude. Bottom left: fluid particles coloured by density.

The SPH model of the tension-leg platform consists of four vertical cylinders that, in real life, are mostly filled with air and keep the platform afloat. The cylinders are connected by pontoons. The top deck is modelled by a thin layer of particles. The platform has a mass of 4×10^7 kg, and a surface area of 72 m x 72 m. The centre-of-mass is located at $\mathbf{x}_1 = [\ 426\ \text{m}, 0, 9\ \text{m}\ ]^T$. The platform is tied to the sea bed with eight tension legs, each of which is modelled as a perfect spring with a spring

constant 4 x 10^7 N/m and a nominal length of 500 m. The moments-of-inertia are: $I_{\xi\xi}$ = 3.7 x 10^{10} kg m^2, $I_{\eta\eta}$ = 3.5 x 10^{10} kg m^2, $I_{\zeta\zeta}$ = 3.3 x 10^{10} kg m^2.

The two ships are modelled in an identical way in the SPH simulation. Both are assumed to have a length of 60 m and a width of 16 m. The mass of each ship is 4.3 x 10^6 kg. The moments of inertia along the principal axes are: $I_{\xi\xi}$ = 2.2 x 10^9 kg m^2, $I_{\eta\eta}$ = 4.3 x 10^8 kg m^2, $I_{\zeta\zeta}$ = 2.2 x 10^9 kg m^2, where ξ is measured along the length of the ship, η runs along the width of the ships, and ζ is the vertical coordinate. The centre-of-mass is located half-way the length, at 30 m behind the bow, at a height of 1 m below the nominal sea level. The two ships have a different orientation: one ship's bow ('object 3') is directed perpendicular to the incident wave, whereas the other ship's bow ('object 2') is directed parallel to the incident wave.

B. Simulation results

Snapshots of the particle positions after 56 s of simulation time, when the extreme wave arrives at the platform, are shown in Figure 6. These snapshots give a qualitative picture of the resulting motion of the three floating objects. It can be observed that the three objects are all brought into motion around the time the extreme wave passes. The ships, which have a lower mass and moment-of-inertia compared to the platform, are given the highest rotation and displacement by the passing wave. For example, from the side view it is clear that the transverse ship ('Object 2') is subject to a considerable roll motion. The position and the orientation of the platform remain relatively steady, thanks to the tension legs that are tied to the sea bed.

A collision take place between Object 2 and the platform at approximately 57 s, and another collision between Object 3 and the platform takes place around 59 s. The collisions ensure that the three objects do not penetrate each other. The extreme wave reaches the beach downstream of the platform at approximately 80 seconds. In the period afterwards, the tension-leg platform is gradually brought back to its equilibrium position, while only small-amplitude waves pass the three objects. These small waves do not have the energy to drive the three objects apart, so they remain close together for the remainder of the simulation.

Quantitative information can be extracted from the displacement data of the floating objects. In Figure 7, we show the vertical and horizontal position (the x-coordinate, to be precise) of the centre-of-mass of each of the objects. Object 1 is the tension leg platform, whose centre-of-mass is initially located at (x, z) = (426 m, 9 m). It moves some 37 m to the right in the course of the simulation, and some 3 m in the downwards vertical direction; the tension legs pull the platform down into the water as it moves away from its equilibrium position. The centre-of-mass of the transverse ship 'Object 2', initially located at (x, z) = (350 m, –1 m), is displaced within a range of 60 m in the horizontal direction and 30 m in the vertical direction. Thus, the extreme wave clearly has a much greater effect on the ship than on the platform, as could be expected. Also the other ship, 'Object 3', moves by more than 75 m in the course of the simulation, although its vertical motion is limited to a band of approximately 20 m.

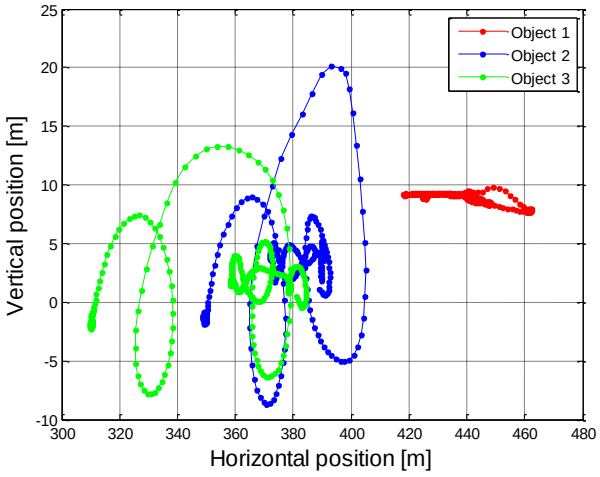

Figure 7. Result from the SPH simulation with a tension-leg platform surrounded by two ships (coarse resolution): trajectories of the centre-of-mass of the three objects in the course of time. The distance between two dots represents a time instant of 0.4 s.

VI. CONCLUSION

We have presented a new method to generate multi-modal and multi-directional sea waves within the framework of SPH. The new method has been used to generate an extreme wave reminiscent of the New Year Wave that was recorded at the Draupner platform in 1995. As a proof-of-concept, the method has been used to simulate the motion of a tension-leg platform surrounded by two ships. The latter simulation also includes new models for rigid-body motion and elastic collisions, both of which have been described in this paper as well.

REFERENCES

[1] G. Eason, B. Noble, and I. N. Sneddon, "On certain integrals of Lipschitz-Hankel type involving products of Bessel functions," Phil. Trans. Roy. Soc. London, vol. A247, pp. 529–551, April 1955. *(references)*

[2] J. Clerk Maxwell, A Treatise on Electricity and Magnetism, 3rd ed., vol. 2. Oxford: Clarendon, 1892, pp.68–73.

[3] I. S. Jacobs and C. P. Bean, "Fine particles, thin films and exchange anisotropy," in Magnetism, vol. III, G. T. Rado and H. Suhl, Eds. New York: Academic, 1963, pp. 271–350.

[4] K. Elissa, "Title of paper if known," unpublished.

[5] R. Nicole, "Title of paper with only first word capitalized," J. Name Stand. Abbrev., in press.

[6] Y. Yorozu, M. Hirano, K. Oka, and Y. Tagawa, "Electron spectroscopy studies on magneto-optical media and plastic substrate interface," IEEE Transl. J. Magn. Japan, vol. 2, pp. 740–741, August 1987 [Digests 9th Annual Conf. Magnetics Japan, p. 301, 1982].